IVYSPRING INTERNATIONAL PUBLISHER

Theranostics

2018; 8(4): 990-1004. doi: 10.7150/thno.22465

Research Paper

O_2-generating MnO_2 nanoparticles for enhanced photodynamic therapy of bladder cancer by ameliorating hypoxia

Tingsheng Lin[1*], Xiaozhi Zhao[1*], Sheng Zhao[2], Hang Yu[1], Wenmin Cao[1], Wei Chen[1], Hui Wei[2✉], and Hongqian Guo[1✉]

1. Department of Urology, Drum Tower Hospital, Medical School of Nanjing University, Institute of Urology, Nanjing University, Nanjing, Jiangsu 210008, China;
2. Department of Biomedical Engineering, College of Engineering and Applied Sciences, Collaborative Innovation Center of Chemistry for Life Sciences, Nanjing National Laboratory of Microstructures, Nanjing University, Nanjing, Jiangsu 210093, China.

* These authors contributed equally.

✉ Corresponding authors: dr.ghq@nju.edu.cn. Tel: +86-136-0517-1690 (H.G.). weihui@nju.edu.cn. Web: http://weilab.nju.edu.cn. Fax: +86-25-83594648. Tel: +86-25-83593272 (H.W.).

Received: 2017.08.21; Accepted: 2017.10.21; Published: 2018.01.01

Abstract

Photodynamic therapy (PDT) is an emerging effective treatment for cancer. However, the great promise of PDT for bladder cancer therapy has not yet been realized because of tumor hypoxia. To address this challenge, we fabricated O_2-generating HSA-MnO_2-Ce6 NPs (HSA for human serum albumin, Ce6 for chlorin e6, and NPs for nanoparticles) to overcome tumor hypoxia and thus enhance the photodynamic effect for bladder cancer therapy.

Methods: The HSA-MnO_2-Ce6 NPs were prepared. We investigated the O_2 generation of NPs *in vitro* and *in vivo*. The orthotopic bladder cancer model in C57BL/6 mice was established for *in vivo* study, and dual-modal imaging of NPs were demonstrated. Therapeutic efficacy of NPs for bladder cancer was evaluated.

Results: HSA-MnO_2-Ce6 NPs had an excellent performance in generating O_2 *in vitro* upon reaction with H_2O_2 at endogenous levels. Moreover, $^1O_2$ generation was increased two-fold by using HSA-MnO_2-Ce6 NPs instead of HSA-Ce6 NPs in the presence of H_2O_2 under 660 nm laser irradiation. *In vitro* cell viability assays showed that HSA-MnO_2-Ce6 NPs themselves were non-toxic but greatly enhanced PDT effects on bladder cancer cells under laser irradiation. *In vivo* near-infrared (NIR) fluorescence and magnetic resonance (MR) imaging suggested the excellent bladder tumor-targeting property of HSA-MnO_2-Ce6 NPs. O_2 content in orthotopic bladder cancer was increased 3.5-fold after injection of HSA-MnO_2-Ce6 NPs as compared with pre-injection. Given the excellent tumor-targeting ability and negligible toxicity, HSA-MnO_2-Ce6 NPs were then used to treat orthotopic bladder cancer by PDT. The PDT with HSA-MnO_2-Ce6 NPs showed remarkably improved therapeutic efficacy and significantly prolonged lifetime of mice as compared with controls.

Conclusion: This study not only demonstrated the great potential of HSA-MnO_2-Ce6 NPs for bladder cancer photodynamic ablation but also provided a new therapeutic strategy to overcoming tumor hypoxia.

Key words: enhanced photodynamic therapy, manganese dioxide (MnO_2), orthotopic bladder cancer, oxygen generation, redox active nanoparticles, tumor hypoxia, tumor microenvironment.

Introduction

Bladder cancer, arising from the epithelial lining (i.e., the urothelium) of a urinary bladder, is one of the most common malignancies of the urinary system.[1-3] Current treatments for bladder cancer include

surgery, radiotherapy, and chemotherapy, but the mortality is still high.[4] Therefore, more efficient strategies are needed to improve therapeutic efficacy for bladder cancer.

Type II photodynamic therapy (PDT), a form of phototherapy involving light and a photosensitizer, is used in conjunction with molecular oxygen (O_2) to produce singlet oxygen ($^1O_2$) that leads to cellular necrosis and apoptosis.[5-8] It has shown high treatment efficacy for tumor ablation, with minimal invasiveness, reduced long-term mortality, and capability to trigger antitumor immune responses.[9-23] Recent studies have indicated that PDT is a promising treatment strategy for bladder cancer.[5,24] Patients could be intravenously injected with photosensitizers (such as 5-aminolevulinic acid, hexaminolevulinate or Radachlorin®), then the bladder is irradiated with a laser to produce $^1O_2$ for tumor ablation (the laser fiber could be inserted into the bladder via the urethra).[3,25] However, the full promise of PDT for bladder cancer in the clinic has not yet been realized due to its low treatment efficacy.[25-27] This is probably due to the hypoxic microenvironment in bladder cancer tissues, which in turn limits the essential O_2 supply during PDT.[28-30]

To enhance the efficacy of PDT for bladder cancer, it is necessary to develop effective strategies to supply adequate O_2 for ameliorating hypoxia. One strategy to address this issue is to deliver additional O_2 into the hypoxic tumor tissues by hyperbaric oxygen inhalation or by using O_2-containing nanomaterials.[31,32] More recently, another smart strategy was proposed to alleviate tumor hypoxia by *in situ* producing O_2, which took advantage of tumor-specific microenvironment characteristics (i.e., higher level of H_2O_2 and more acidic pH).[33-37] Since the hypoxia-driven metabolic changes in bladder cancer cells also produce higher levels of H_2O_2 and promote acidosis,[38-41] we reason that the efficacy of PDT for bladder cancer would be significantly enhanced by *in situ* producing O_2 from H_2O_2.

In this work, we reported an effective strategy to improve the efficacy of PDT for bladder cancer by ameliorating hypoxia with O_2-generating HSA-MnO_2-Ce6 NPs (Scheme 1). Redox-active MnO_2 NPs were chosen due to their high reactivity toward H_2O_2 to produce O_2. MnO_2 NPs themselves would be decomposed under acidic pH to release Mn^{2+} for magnetic resonance (MR) imaging.[42-45] Ce6 (chlorin e6), an excellent PDT photosensitizer with a high $^1O_2$ quantum yield and near-infrared (NIR) fluorescence, and HSA (human serum albumin), a well-known drug carrier protein with excellent biocompatibility, were used together with MnO_2 to fabricate HSA-MnO_2-Ce6 NPs.[46-49] *In vitro* study revealed that the NPs exhibited remarkable PDT efficacy due to their high oxygen production efficiency. *In vivo* study, using an orthotopic bladder cancer mouse model, demonstrated that abundant O_2 was *in situ* generated in the tumor tissue after systemic intravenous (i.v.) injection of HSA-MnO_2-Ce6 NPs. More notably, when PDT treatment of orthotopic bladder cancer was carried out using HSA-MnO_2-Ce6 NPs, more complete ablation of bladder cancer was achieved and significantly prolonged lifetime of mice was observed.

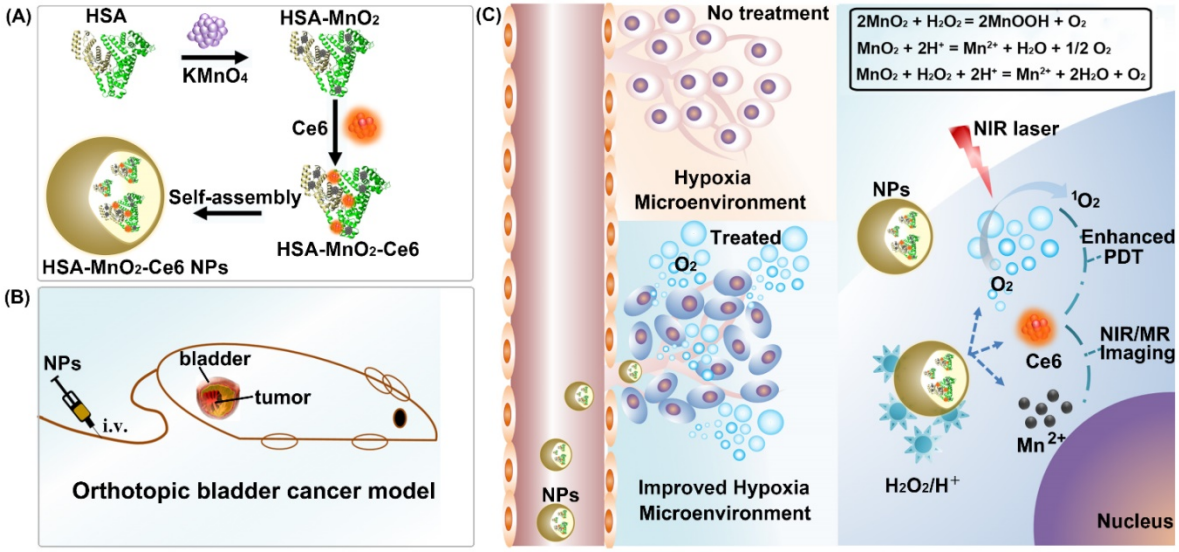

Scheme 1. Schematic representation of the synthesis of HSA-MnO_2-Ce6 NPs (a) and their application in enhanced PDT therapy for orthotopic bladder cancer by ameliorating hypoxia (b and c). HSA: human serum albumin; Ce6: chlorin e6; NPs: nanoparticles; i.v.: intravenous.

Materials and Methods

Chemicals and materials

HSA was obtained from CSL Behring AG (Switzerland). Chlorin e6 (Ce6) was from Frontier Scientific (Logan, Utah, USA). Potassium permanganate ($KMnO_4$) and hydrogen peroxide (H_2O_2, 30 wt%) were from Sino pharm Chemical Reagent Co. (China). 1-ethyl-3-(3-dimethylaminopropyl) carbodiimide (EDC) and N-hydroxysuccinimide (NHS) were from J&K Scientific Ltd. (China). 4',6-diamidino-2-phenylindole dihydrochloride (DAPI) and Singlet Oxygen Sensor Green (SOSG) probe were from Molecular Probes (USA). 1640 medium was from Gibco (Grand Island, NY, USA). The cell counting kit-8 (CCK-8) was from Dojindo Laboratories (Japan). 1×Phosphate buffer solution (PBS) and deionized water were used in the experiments. All C57BL/6 female mice (18-20 g) were obtained from Yangzhou University Medical Center.

Preparation of HSA-MnO_2 NPs, HSA-Ce6 NPs, and HSA-MnO_2-Ce6 NPs

HSA-coated MnO_2 NPs (HSA-MnO_2 NPs) were prepared as follows.[50] In brief, 6.32 mg $KMnO_4$ dispersed in 0.6 mL water was drop-wise added into 50 mg HSA dispersed in 1.4 mL PBS. The mixture was stirred at 37 °C for 2 h to obtain HSA-MnO_2 NPs.

HSA-MnO_2-Ce6 NPs were then prepared follows. First, the activated 4.5 mg Ce6-NHS ester mixture (4.5 mg Ce6, 6.9 mg EDC, and 3.7 mg NHS added into 1 mL of DMSO, stirred for 8 h) was added into 2 mL HSA-MnO_2 NPs solution. The mixture was then diluted to 10 mL by adding 7 mL PBS (V_{DMSO}:$V_{aqueous}$ = 1:9). The reaction mixture was stirred at room temperature for 20 h to allow the conjugation of Ce6 onto HSA-MnO_2 NPs via the interaction between the carboxylic groups of Ce6 and the amine groups of the lysine residues within HSA. Due to the hydrophobic property of Ce6, the conjugates self-assembled into HSA-MnO_2-Ce6 NPs.

HSA-Ce6 NPs were prepared using HSA instead of HSA-MnO_2 NPs, under conditions otherwise identical to those used for preparing HSA-MnO_2-Ce6 NPs.

The above three NPs solutions were further purified by removing free small molecules with an ultrafiltration membrane (molecular weight ~30 kDa). They were then filtered through a filter membrane (pore size 0.22 μm). The NPs dispersions were stored at 4 °C for further use.

Characterization of HSA-MnO_2 NPs, HSA-Ce6 NPs, HSA-MnO_2-Ce6 NPs

The morphology and particle size of NPs were measured by transmission electron microscopy (TEM) (Hitachi H-7650). The NPs were dried on a copper grid coated with amorphous carbon and observed at 200 kV. The hydrodynamic size and zeta potential of the NPs were measured by dynamic light scattering (DLS; Brookhaven Instruments, USA). The colloidal stability of HSA-MnO_2-Ce6 NPs was investigated in PBS (pH 7.4) at 37 °C by measuring their mean diameter with DLS. A UV–visible spectrophotometer (UV2450, Shimadzu Corp.) was used to measure the UV–visible spectra of NPs. Powder X-ray diffraction measurements were collected on Rigaku Ultima Diffractometer at 40 kV and 40 mA with a scan rate of 2°/min using Cu Kα radiation. Concentrations of MnO_2 were measured using inductively coupled plasma atomic emission spectroscopy (Thermo). The concentration of Ce6 was calculated from its characteristic absorption peak at 665 nm. The final concentrations of Ce6 and Mn in HSA-MnO_2-Ce6 NPs stock solution were 500 μg/mL and 10 mM, respectively.

In vitro O_2 and $^1O_2$ generation

O_2 generated by HSA-MnO_2-Ce6 NPs was measured in a sealed chamber coupled with an oxygen electrode (Dissolved Oxygen Meter, AZ-8402, Guangdong, China) at 37 °C. HSA-MnO_2-Ce6 NPs (200 μM MnO_2) were dispersed in PBS, and the pre-dissolved O_2 was removed by bubbling with N_2 for 30 min. H_2O_2 (100 μM and 500 μM) was then injected into the chamber and the generated O_2 was recorded at set time points. The O_2 generation from H_2O_2 solution (100 μM) at different pH (6.5 and 7.4) by using HSA-MnO_2-Ce6 NPs (200 μM MnO_2) was also studied.

The $^1O_2$ generation under laser irradiation in the absence or presence of 100 μM H_2O_2 solution by HSA-Ce6 and HSA-MnO_2-Ce6 NPs (1 μg/mL Ce6) was measured with an SOSG probe. In brief, SOSG dissolved in methanol was added to the samples to measure $^1O_2$ generation, which were irradiated with a 660-nm laser (5 mW/cm^2) in N_2 atmosphere. The generated $^1O_2$ was determined by measuring recovered SOSG fluorescence at 525 nm under 494 nm excitation.

In vitro MR imaging with HSA-MnO_2-Ce6 NPs

HSA-MnO_2-Ce6 NPs at different Mn concentrations (0, 0.05, 0.1, 0.2, and 0.4 mM) in PBS were incubated at different pH (6.5 and 7.4) for 12 h before MR imaging. MR imaging was performed with a 7.0 T MRI scanner (BioSpec 70/20USR, Bruker, Germany). The longitudinal (T1) phantom images as well as relaxation time (T1) were recorded.

In vitro cellular uptake behavior of HSA-MnO_2-Ce6 NPs

Mouse bladder cancer cells (MB-49) were cultured in 1640 medium containing 10% fetal bovine serum, 1% penicillin, and 1% streptomycin at 37 °C in a CO_2 incubator. MB-49 cells were seeded into 24-well chambers with cover glass at 2×10^4 cells/well and cultured for 24 h. To evaluate the cellular uptake of NPs, fresh medium containing HSA-Ce6 or HSA-MnO_2-Ce6 NPs (2.5 μg/mL Ce6) was added. After 6 h co-incubation, cells were washed with PBS three times and fixed with 4% paraformaldehyde solution for 20 min, then stained for 15 min with DAPI. Confocal laser scanning microscopy (Leica TCS SP5, Germany) was used to observe fluorescence in cells.

For cellular uptake experiments by flow cytometry, MB-49 cells were seeded in 6-well plates at 5×10^5 cells/well. The treatment was the same as for the above cell uptake experiments. Then, cells were washed with PBS three times and centrifuged, re-suspended in 500 μL PBS, and analyzed by flow cytometry. The fluorescence of Ce6 was collected on the APC-A channel.

Cytotoxicity study with HSA-MnO_2-Ce6 NPs

To evaluate the cytotoxicity of HSA-MnO_2-Ce6 NPs, the hemolytic effect of HSA-MnO_2-Ce6 NPs was first studied. Whole blood was collected from C57BL/6 mice. Red blood cells were isolated by centrifugation, then washed three times with PBS. The cells were treated with HSA-MnO_2-Ce6 NPs, then centrifuged, and the absorbance of supernatants at 540 nm was measured. A sample treated with 1% Triton-X 100 (Sigma) in PBS was used as a 100% hemolysis standard.

The cytotoxicity of HSA-MnO_2-Ce6 NPs toward MB-49 cells was investigated by using CCK-8 assay as follows. The cells were seeded at 1×10^4 cells/well in 96-well plates with 1640 medium containing 10% fetal bovine serum. After 24 h, the medium was replaced with 100 μL fresh medium containing different concentrations of HSA-MnO_2, HSA-Ce6 or HSA-MnO_2-Ce6 NPs. After 24 h, CCK-8 assay was used to evaluate cell viability.

The photo-cytotoxicity of HSA-MnO_2-Ce6 NPs was investigated by CCK-8 as follows. The cells were seeded at 1×10^4 MB-49 cells/well in a 96-well plate using 1640 medium containing 10% FBS. After 24 h incubation, the medium was replaced with 100 μL fresh medium containing different concentrations of HSA-MnO_2 NPs, HSA-Ce6 NPs or HSA-MnO_2-Ce6 NPs. 6 h later, cells were washed with PBS and 100 μL fresh medium was added, then the cells were irradiated with a 660 nm laser (5 mW/cm^2) for 30 min under N_2 atmosphere. After 24 h incubation, CCK-8 assay was used to evaluate the cell viability.

Establishment of an orthotopic bladder cancer model in C57BL/6 mice

All mice received care following the guidelines of the Care and Use of Laboratory Animals and their use followed the terms of the Institutional Animal Care regulations and Use Committee of Nanjing University. All animal experiments were approved by the Administration Committee of Experimental Animals in Jiangsu Province and the Ethic Committee of Nanjing University.

An orthotopic bladder cancer model was established with minimal invasiveness in C57BL/6 mice.[51] A small cut (~2 mm) was made into the skin of the lower abdomen, and the bladder was found and clamped carefully by using smooth forceps. MB-49 cells (5×10^6) were injected into the bladder wall using a 1 mL syringe. Tumor growth in the bladder was confirmed visually 9 days later.

Dual-modal imaging of HSA-MnO_2-Ce6 NPs

For near-infrared (NIR) fluorescence imaging, HSA-Ce6 or HSA-MnO_2-Ce6 NPs (2.5 mg/kg Ce6) were administered via tail vein injection when the mouse bladder tumor size was ~110 mm^3. For comparison, HSA-MnO_2-Ce6 NPs (2.5 mg/kg Ce6) were administered via tail vein injection in normal mice. At 2, 12, 24, and 48 h after injection, images were obtained by an *in vivo* imaging system (IVIS Lumina, USA). Then, mice were sacrificed and the organs (heart, liver, spleen, lung, kidney, intestine, and bladder) were collected for imaging and semi-quantitative biodistribution analysis by using the imaging system. Emission spectra of Ce6 (710–900 nm) were obtained at a fixed excitation wavelength of 675 nm. Dye accumulation and retention in organs was evaluated by using the NIR analysis software Living Image 4.2.

MRI was performed with a 7.0 T MRI scanner (BioSpec 70/20USR, Bruker, Germany). The T1-weighted MR images of bladder tumors were examined at 0, 4, and 24 h after intravenous injection of PBS or HSA-MnO_2 or HSA-MnO_2-Ce6 NPs (4.35 mg/kg MnO_2) into mice with orthotopic bladder cancer. MR scanning parameters were: T1 propeller sequence, 1 mm slice thickness, TR/TE 789.8/10 ms, 3.0 cm field of view, and matrix 256(a). The relative signal intensity (RSI) was calculated from the ratio of signals in the bladder tumor area to those in normal tissue areas.

Effect of HSA-MnO2-Ce6 NPs on tumor oxygenation

The effect of HSA-MnO_2-Ce6 NPs on oxygen content in bladder cancer was evaluated by using an *in vivo* oxygen probe (O_2 Microsensor, Unisense, Denmark). Since the oxygen content probably varied with the depth of tumor tissue, the oxygen probe was inserted into bladder cancer tissues with a fixed depth of 2 mm. Then, the oxygen content of bladder tumors was measured at 0 h (pre-injection), 4 h, and 24 h after intravenous injection of HSA-MnO_2-Ce6 NPs solution (8.7 mg/kg MnO_2) or PBS. The relative tumor oxygen was calculated from the ratio of oxygen content in bladder cancer post- and pre-injection of the NPs.

To further demonstrate the ability of HSA-MnO_2-Ce6 NPs to improve the hypoxic environment of bladder cancer, a hypoxyprobe (pimonidazole, Hypoxyprobe-1 plus kit, Hypoxyprobe Inc.) was used to observe pimonidazole-stained hypoxic tumor areas visually. Mice with orthotopic bladder cancer were intravenously injected in the tail vein with PBS or HSA-MnO_2-Ce6 NPs (8.7 mg/kg MnO_2). After a predetermined time, bladders were surgically excised 90 min after intraperitoneal injection with pimonidazole hydrochloride (60 mg/kg). Frozen sections of bladders were created. The tumor sections were incubated with mouse anti-pimonidazole antibody (dilution 1:100, Hypoxyprobe Inc.) and Alex 488-conjugated goat anti-mouse secondary antibody (dilution 1:200, Jackson Inc.) as instructed. Nuclei were stained with DAPI.

Therapeutic efficacy of HSA-MnO_2-Ce6 NPs in orthotopic bladder cancer model

The bladder cancer volume was calculated using the formula $a*(b/2)^2$, where a is the major axis and b the minor axis, upon exposure of the bladder. When the tumor size was ~125 mm^3, treatments were started. Mice with orthotopic bladder cancer were divided into seven groups (4 mice in each group): PBS, HSA-MnO_2 NPs, HSA-MnO_2 NPs with laser irradiation, HSA-Ce6 NPs, HSA-Ce6 NPs with laser irradiation, HSA-MnO_2-Ce6 NPs, and HSA-MnO_2-Ce6 NPs with laser irradiation. Mice were injected with PBS or NPs via the tail vein (5 mg/kg Ce6, 8.7 mg/kg MnO_2). The time 24 h after injection was designated as day 0. For laser irradiation treatment, bladders were exposed visually by making a small cut (about 2 mm) into the skin of the lower abdomen, then bladders were directly exposed to the laser. (Note, for future clinical translation, optical fibers plus endoscope techniques definitely will be more useful since the laser fiber can be inserted into the bladder via the urethra for PDT in bladder cancer). Bladders were irradiated by 660 nm laser for 15 min (200 mW/cm^2) after day 0. The photodynamic effect of HSA-MnO_2-Ce6 NPs on bladder cancer was detected on day 3 by contrast enhanced ultrasound (CEUS) and ultrasonography (US) imaging. The CEUS and US images were recorded after intravenous injection of microbubbles (SonoVue) according to a clinical CEUS protocol. CEUS, a diagnostic tool used in the clinic, is based on ultrasonography and uses stabilized microbubbles to improve the echogenicity of blood flow.

Urinary red blood cell counts were measured to evaluate the photodynamic effect on hematuria. Urine samples of the PBS, HSA-Ce6 NPs and HSA-MnO_2-Ce6 NPs groups with laser irradiation were collected on days 0, 6 and 12. Red blood cell counts were analyzed at the Laboratory Medicine of Nanjing Drum Tower Hospital.

The body weight of each mouse was recorded. On day 12, mice were sacrificed, and the tumor size in the bladder was measured. Photographs were taken using a high-quality camera, and bladders were collected for hematoxylin and eosin (HE) staining and TUNEL assay.

In vivo toxicity of HSA-MnO_2-Ce6 NPs

To further assess the *in vivo* safety of HSA-MnO_2-Ce6 NPs, blood samples and organs of healthy C57BL/6 mice injected with PBS or HSA-MnO_2-Ce6 NPs (5 mg/kg Ce6, 8.7 mg/kg MnO_2) were harvested and analyzed on day 7 post-injection. From blood samples, hepatic function was evaluated by alanine aminotransferase (ALT) and aspartate aminotransferase (AST) levels and renal function by urea nitrogen (UREA) and creatinine (CREA) levels. The normal ranges of these parameters for female mice (<1 year old) are: ALT, 14-67 U/L; AST, 34-114 U/L; UREA, 7-16 mM; and CREA, 1545 μM.[52] Five organ tissues (heart, liver, spleen, lung, and kidney) were collected for HE staining.

H_2O_2 concentration in bladder cancer tissues

The H_2O_2 concentration in bladder cancer tissues was measured using a Hydrogen Peroxide Assay Kit (Nanjing Jiancheng Bioengineering Institute, China). Tumor tissues were collected form mice bearing orthotopic bladder cancer. PBS was added to tumor tissues to prepare homogenate. The supernatant was then collected after centrifugation. The measured H_2O_2 concentration in bladder cancer tissues was 715.7±304.6 μM, which was high enough to generate O_2 in tumor by reacting with MnO_2.

Statistical analysis

Statistical analysis involved two-sided Student *t* test for two groups and one-way ANOVA for

multiple groups. $P < 0.05$ was considered statistically significant.

Results and Discussion

Preparation and characterization of HSA-MnO_2-Ce6 NPs

The synthesis of HSA-MnO_2-Ce6 NPs is illustrated in Scheme 1. First, HSA-MnO_2 NPs were obtained via the reduction of $KMnO_4$ with HSA.[50] Next, the carboxylic groups of Ce6 were conjugated with the amine groups of the lysine residues within HSA to form HSA-MnO_2-Ce6 NPs.[53] The molar ratio of Ce6 to MnO_2 in HSA-MnO_2-Ce6 NPs was 0.084:1.

The formation of HSA-MnO_2-Ce6 NPs as well as HSA-MnO_2 and HSA-Ce6 NPs was investigated by measuring their UV–visible absorption spectra. Compared to HSA-Ce6 NPs, HSA-MnO_2-Ce6 NPs showed a new UV–visible absorption band around 300–400 nm (Figure 1a), which could be attributed to the surface plasmon band of MnO_2.[54] DLS (dynamic light scattering) revealed the mean size of HSA-MnO_2, HSA-Ce6, and HSA-MnO_2-Ce6 NPs as 18.5±4.8 nm, 112.8±7.4 nm and 118.6±8.1 nm, respectively (Figure 1b). The PDI (polydispersity index) of HSA-MnO_2, HSA-Ce6, and HSA-MnO_2-Ce6 NPs was 0.091±0.013, 0.101±0.012, and 0.104±0.019, respectively. All three NPs were generally spherical in shape with good mono-dispersity (Figure 1c) and their zeta potentials were -21.3±1.5 mV, -27.1±1.6 mV and -24.8±1.0 mV, respectively (Figure S2). In 30 days, the size of HSA-MnO_2-Ce6 NPs in PBS at 37 °C remained constant (~120 nm) (Figure S3), indicating their excellent colloidal stability.

In vitro O_2 and $^1O_2$ generation

O_2 could be efficiently generated from H_2O_2 with MnO_2 as follows (Equation 1-3):

$$2MnO_2 + H_2O_2 = 2MnOOH + O_2 \quad (1)$$

$$MnO_2 + 2H^+ = Mn^{2+} + H_2O + 1/2\ O_2 \quad (2)$$

$$MnO_2 + H_2O_2 + 2H^+ = Mn^{2+} + 2H_2O + O_2 \quad (3)$$

We first tested whether HSA-MnO_2-Ce6 NPs could generate O_2 *in vitro* on reaction with H_2O_2 at endogenous levels (100 μM or 500 μM). As shown in Figure 2a, O_2 was efficiently produced from H_2O_2. Longer reaction time or higher concentration of H_2O_2 generated more oxygen (Figure 2a). As indicated in Equation 2 and 3, acidic pH would promote O_2 generation from both MnO_2 and H_2O_2.[45] Thus, we measured the O_2 generation at different pH (6.5 and 7.4) in the presence of HSA-MnO_2-Ce6 NPs (Mn, 200 μM) and H_2O_2 solutions (100 μM). As shown in Figure 2b, the O_2 generation triggered by HSA-MnO_2-Ce6 NPs was faster at pH 6.5 than 7.4, owing to the higher reaction rate of MnO_2 with H_2O_2 under lower pH.

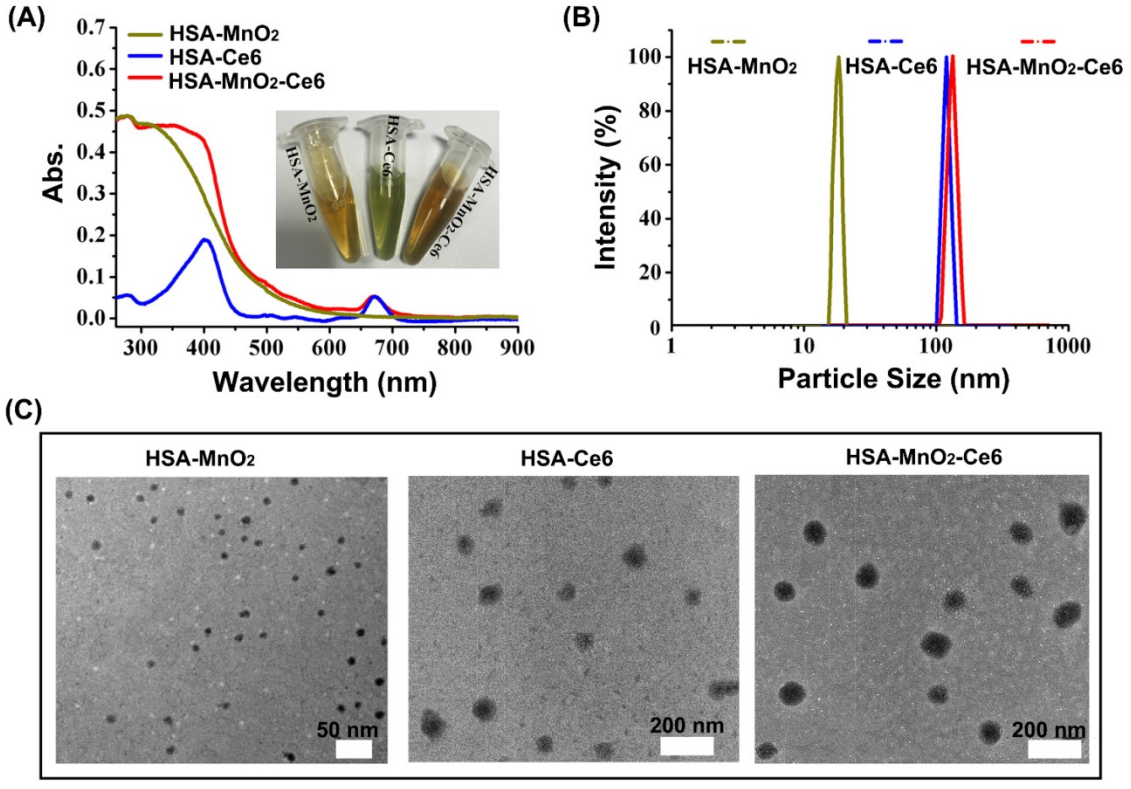

Figure 1. (a) UV–visible absorption spectra of HSA-MnO_2, HSA-Ce6, and HSA-MnO_2-Ce6 NPs in PBS. Inset: photograph of the three NPs dispersed in PBS. (b) Size distribution of the three NPs by DLS. (c) TEM images of the three NPs.

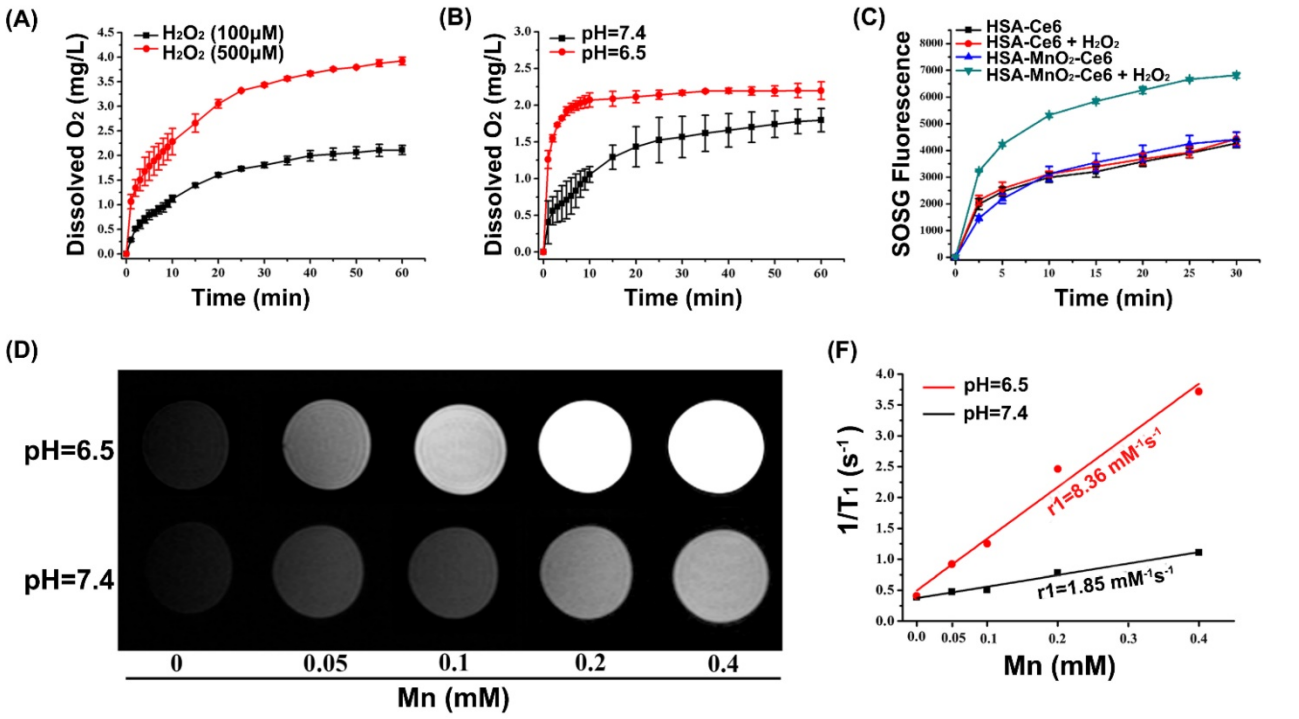

Figure 2. (a) O_2 generation from different H_2O_2 solutions (100 μM and 500 μM) after adding HSA-MnO_2-Ce6 NPs (Mn concentration 200 μM). (b) O_2 generation at different pH values (6.5 and 7.4) from H_2O_2 solutions (100 μM) with HSA-MnO_2-Ce6 NPs. (c) $^1O_2$ generation with HSA-Ce6 and HSA-MnO_2-Ce6 NPs in the absence or presence of H_2O_2 under NIR laser irradiation (660 nm laser, 5 mW/cm^2) under N_2 atmosphere. (d) T1-weighted MR images of HSA-MnO_2-Ce6 NPs of various concentrations at different pH (6.5 and 7.4). (e) Longitudinal relaxation rate (r1) of HSA-MnO_2-Ce6 NPs at pH 6.5 and 7.4. Error bars indicate standard deviations of three independent measurements.

Because oxygen is a key element in the process of PDT, the yield of $^1O_2$ highly depends on O_2 content.[8] Considering the effective O_2 generation in the mixture of H_2O_2 with HSA-MnO_2-Ce6 NPs, we measured the $^1O_2$ generation under laser irradiation in the presence of HSA-MnO_2-Ce6 NPs and H_2O_2 with a singlet oxygen sensor green (SOSG) probe. The $^1O_2$ generation with HSA-Ce6 NPs was measured as a comparison. Both HSA-Ce6 and HSA-MnO_2-Ce6 NPs showed similar $^1O_2$ generation efficiency in the absence of H_2O_2 (Figure 2c). HSA-MnO_2-Ce6 NPs showed a two-fold enhancement of laser-induced $^1O_2$ generation in the presence of H_2O_2, which was due to the MnO_2-triggered generation of O_2. In contrast, $^1O_2$ production with HSA-Ce6 NPs did not differ in the absence or presence of H_2O_2. These results demonstrated that the PDT efficiency of HSA-MnO_2-Ce6 NPs would be significantly improved in the presence of H_2O_2.

In vitro MR imaging with HSA-MnO_2-Ce6 NPs

Because Mn^{2+} is an excellent T1-shortening agent in MRI, we investigated the ability of HSA-MnO_2-Ce6 NPs as contrast agents for MRI. HSA-MnO_2-Ce6 NPs in PBS were incubated at different pH values (6.5 and 7.4) for 12 h before MRI. MRI revealed that the T1-weighted signals were manganese concentration-dependent, with higher concentrations appearing brighter (Figure 2d and 2e). The T1-weighted signal of HSA-MnO_2-Ce6 NPs was much higher at pH 6.5 than 7.4, and the longitudinal relaxivity (r1) value was also increased from 1.85 $mM^{-1}s^{-1}$ at pH 6.5 to 8.36 $mM^{-1}s^{-1}$ at pH 7.4. The much lower relaxivity of the NPs at pH 7.4 was attributed to the higher valence (IV) of manganese and shielding paramagnetic centers inaccessible to water molecules.[42,55,56] The remarkably increased relaxivity of the NPs at pH 6.5 was owing to the decomposition of MnO_2 into paramagnetic Mn^{2+} (Figure S4).

Uptake of HSA-MnO_2-Ce6 NPs by bladder cancer cells

We investigated the cellular uptake efficiency of HSA-Ce6 and HSA-MnO_2-Ce6 NPs. Both NPs were incubated with mouse bladder cancer cells (MB-49) for 6 h and observed by confocal microscopy and flow cytometry. Cells treated with HSA-Ce6 and HSA-MnO_2-Ce6 NPs presented strong Ce6 red fluorescence in the cytoplasm, whereas those treated with PBS showed no Ce6 fluorescence (Figure 3a, 3b, and S5). Flow cytometry results revealed approximately equal cellular uptake of HSA-Ce6 and HSA-MnO_2-Ce6 NPs. Given the abnormally increased concentrations of H_2O_2 in bladder cancer cells,[41] the uptaken HSA-MnO_2-Ce6 NPs could react with endogenous H_2O_2 to produce O_2 *in situ*, which would in turn enable the enhanced PDT for bladder cancer.

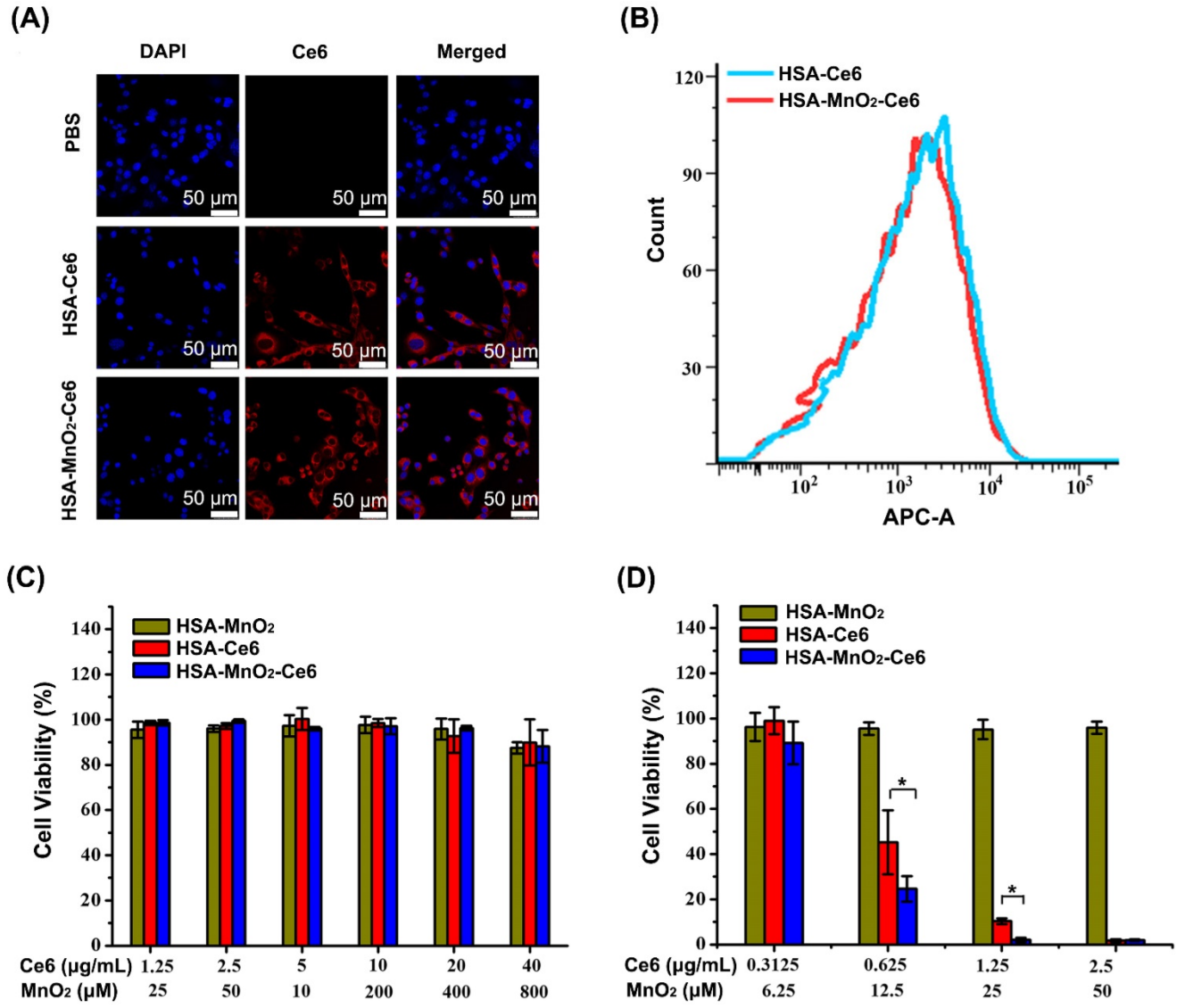

Figure 3. (a) Confocal fluorescence images of MB-49 bladder cancer cells after 6 h incubation with HSA-Ce6 and HSA-MnO_2-Ce6 NPs. Blue fluorescence indicates positive staining of DAPI, and red fluorescence is Ce6. (b) Flow cytometry of MB-49 cells incubated with HSA-Ce6 or HSA-MnO_2-Ce6 NPs. (c) Relative viability of MB-49 bladder cancer cells after incubation with various concentrations of NPs for 24 h. d) Relative viability of MB-49 cells after incubation with NPs under laser irradiation (660 nm, 5 mW/cm^2, 30 min) under N_2 atmosphere. Error bars indicate standard deviations of three independent measurements. (*$p < 0.05$).

Cytotoxicity study with HSA-MnO_2-Ce6 NPs

We first investigated the hemolytic effect of HSA-MnO_2-Ce6 NPs on mice red blood cells. As shown in Figure S5, HSA-MnO_2-Ce6 NPs did not induce significant hemolysis, indicating their good biocompatibility. We next tested the cytotoxicity of HSA-MnO_2, HSA-Ce6, and HSA-MnO_2-Ce6 NPs under the dark condition (Figure 3c). Bladder cancer cells showed no obvious cytotoxicity upon treatment with all three NPs for 24 h under dark.

We further tested the *in vitro* PDT efficiency of the NPs by cell viability assay (Figure 3d). With Ce6 concentrations of 0.625 μg/mL and 1.25 μg/mL, treatment with HSA-MnO_2-Ce6 NPs resulted in 75.35±5.67% and 97.92±0.93% cell death, and treatment with HSA-Ce6 NPs resulted in 54.76±14.17% and 89.70±1.22% cell death. In addition, HSA-MnO_2 NPs showed no obvious photocytotoxicity for cells. These *in vitro* results demonstrated that HSA-MnO_2-Ce6 NPs exhibited the best PDT effects for bladder cancer cells.

Dual-modal imaging of HSA-MnO_2-Ce6 NPs in orthotopic bladder cancer model

After the establishment of the orthotopic bladder cancer model in C57BL/6 mice (Figure S6),[51] the distribution of HSA-Ce6 and HSA-MnO_2-Ce6 NPs in C57BL/6 mice was evaluated by NIR imaging. The fluorescence of Ce6 distributed widely throughout the mouse body after 2 h injection of the NPs (Figure 4a and 4c). Subsequently, HSA-Ce6 and HSA-MnO_2-Ce6

NPs showed remarkable accumulation in the bladder area (black dotted circles) in mice with orthotopic bladder cancer at 24 h and 48 h. In contrast, the mice with a normal bladder did not show obvious accumulation of HSA-MnO_2-Ce6 NPs in the bladder area. *Ex vivo* imaging of excised major organs at 48 h post-injection were investigated (Figure 4b and 4d). Strong Ce6 fluorescence intensity appeared in tumor-bearing bladders, with barely no fluorescence intensity in normal bladders, which indicated excellent *in vivo* tumor targeting of the NPs. To further prove high tumor uptake of the NPs, we measured stained bladder cancer slices. As the confocal images showed, the fluorescence intensity of the NPs was high in bladder cancer tissues, but no fluorescence of NPs was observed in bladder wall (Figure S8). Therefore, this confirmed that the NPs were accumulated in the tumor region instead of in normal bladder tissues.

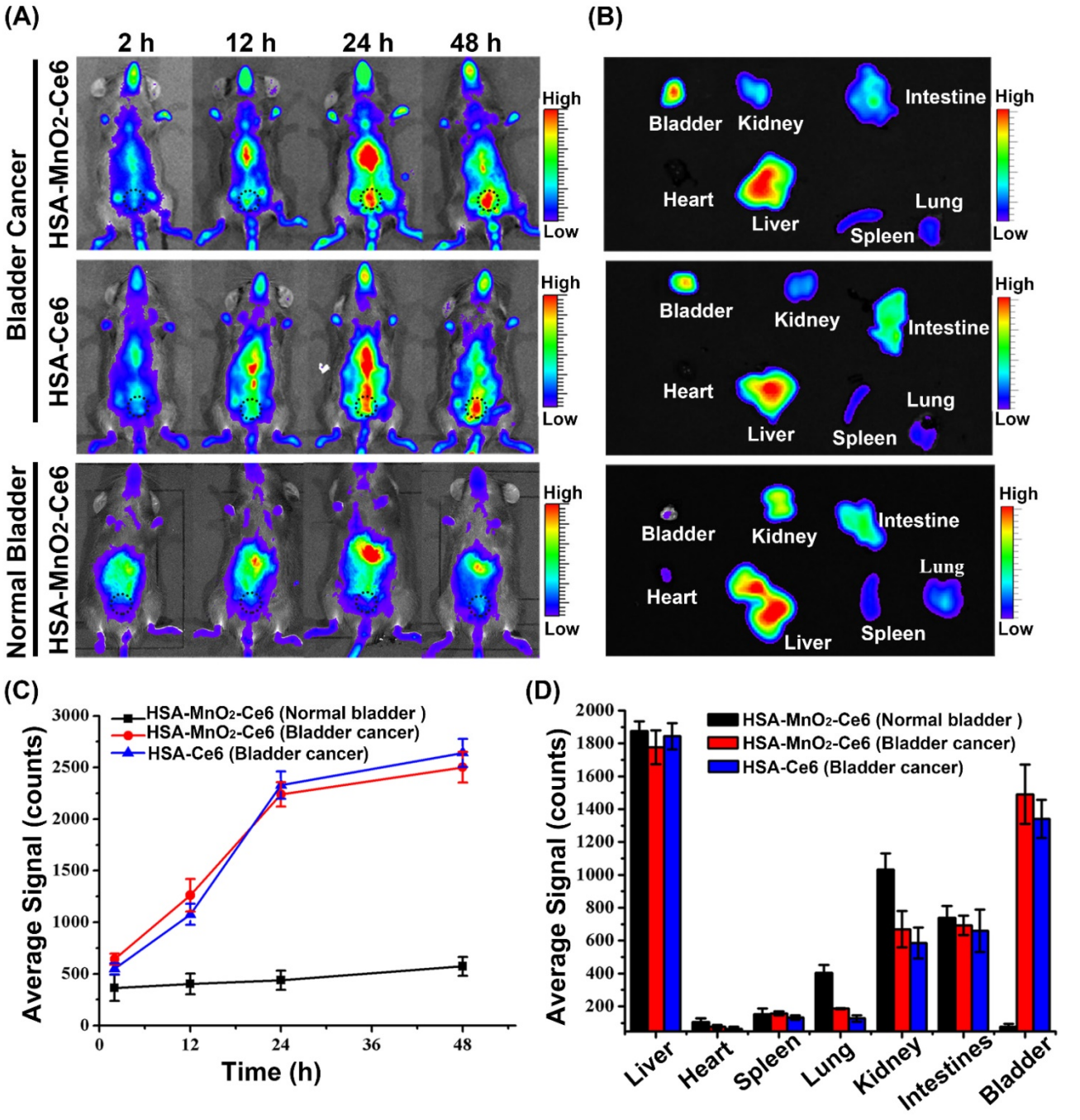

Figure 4. (a) Fluorescence images of C57BL/6 mice with orthotopic bladder cancer injected with HSA-Ce6 or HSA-MnO_2-Ce6 NPs, and normal mice injected with HSA-MnO_2-Ce6 NPs (black dotted circles indicate the bladder area in body surface projection). (b) *Ex vivo* fluorescence images of major organs from mice at 48 h. (c) NIR fluorescence intensities of bladder areas at different time intervals based on *in vivo* fluorescence images shown in (a). (d) Semi-quantitative biodistribution of HSA-Ce6 or HSA-MnO_2-Ce6 NPs in major organs. Error bars indicate standard deviations of three independent measurements.

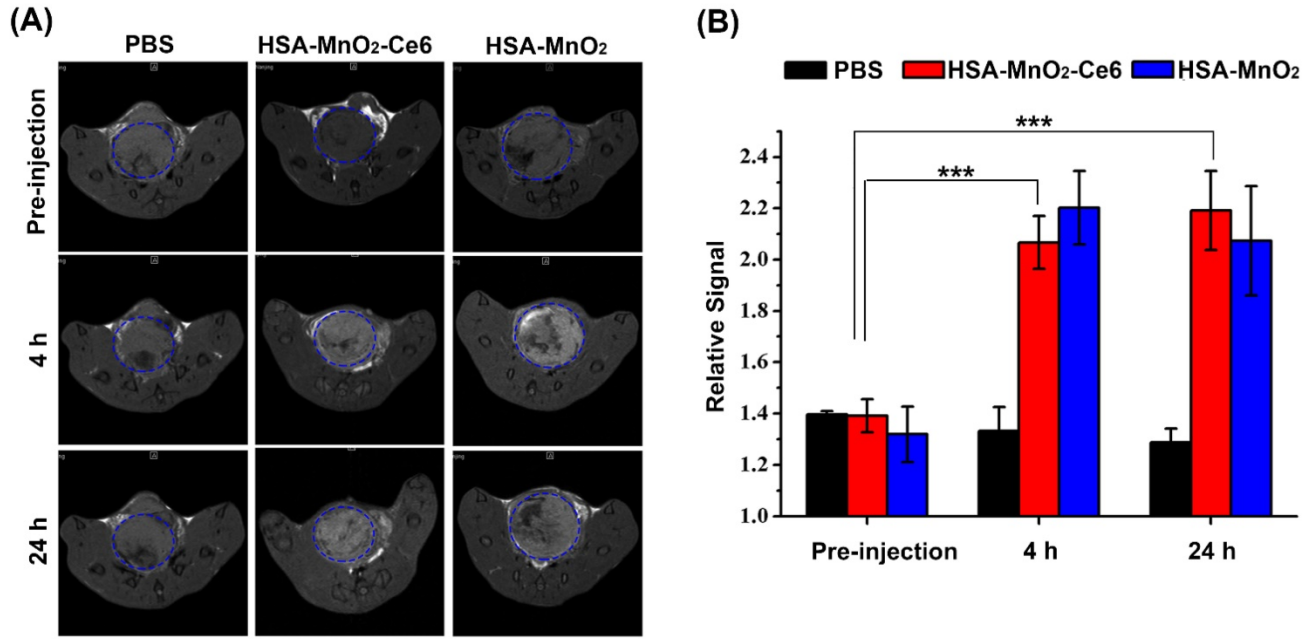

Figure 5. (a) *In vivo* MR images of mice with orthotopic bladder cancer after intravenous injection of PBS or HSA-MnO_2 or HSA-MnO_2-Ce6 NPs at 0, 4, and 24 h. Areas in blue dotted circles represent the tumors in bladders. (b) Relative signal intensity of bladder areas at different time intervals based on MR images shown in (a). Relative signal intensity (RSI) was calculated from the ratio between signals in tumor areas and normal tissue areas (***$p < 0.001$). Error bars indicate standard deviations of three independent measurements.

The T1-weighted MR images of bladder cancers were examined after intravenous injection of PBS or HSA-MnO_2 or HSA-MnO_2-Ce6 NPs into mice with orthotopic bladder cancer at 0, 4, and 24 h (Figure 5a). Bladder cancer tissue and normal tissue did not differ in T1-weighted signal intensity before injection. However, the intensity was significantly increased in the bladder cancer area at 4 h after injection with HSA-MnO_2 NPs (RSI=2.20±0.14) or HSA-MnO_2-Ce6 NPs (RSI=2.06±0.10) at 4 h or 24 h but not with PBS. Moreover, the enhanced T1-weighted signal intensity in bladder cancer areas lasted for 24 h after injection with HSA-MnO_2 NPs (RSI=2.07±0.21) or HSA-MnO_2-Ce6 NPs (RSI=2.19±0.15). The results further confirmed the accumulation of HSA-MnO_2-Ce6 NPs in bladder cancer tissue, which may have great potential for MRI diagnosis of bladder cancer.

Effect of HSA-MnO_2-Ce6 NPs on tumor oxygenation

We evaluated the effect of HSA-MnO_2-Ce6 NPs on oxygen content in orthotopic bladder cancer with an *in vivo* oxygen probe after intravenous injection of HSA-MnO_2-Ce6 NPs solution. Oxygen concentration in bladder cancer tissues increased from 12 μM to 55 μM at 4 h after injection of HSA-MnO_2-Ce6 NPs, and the oxygen concentration remained at 53 μM at 24 h after injection (Figure 6a). In contrast, the oxygen concentration with PBS injection showed no increase at 4 h and 24 h (oxygen level stable at ~15 μM). Quantitative analysis revealed that the tumor oxygen levels at 4 h and 24 h were increased ~3.5-fold after versus before the NPs injection (Figure 6b). The results suggested the excellent O_2 generation by HSA-MnO_2-Ce6 NPs, which significantly improved the hypoxia conditions of bladder cancer.

To further confirm the ability of HSA-MnO_2-Ce6 NPs to improve the hypoxic environment of bladder cancer, we used a hypoxia probe (pimonidazole) to visualize hypoxic tumor areas (Figure 6c and 6d). Clear changes in hypoxia were observed after treatment with HSA-MnO_2-Ce6 NPs. Semi-quantification showed the tumors with PBS treatment remained highly hypoxic (84.26% positive area), with positive pimonidazole staining in most of the viable tumor area. In contrast, the tumors treated with HSA-MnO_2-Ce6 NPs showed significantly decreased hypoxic areas (57.81% and 41.8% at 4 h and 24 h post-injection, respectively). The results could be attributed to the high tumor accumulation of the NPs, which allowed for sustained oxygen generation in the bladder cancer tissues. Such enhanced oxygenation in bladder cancer tissue could favor the increased PDT efficacy *in vivo* to overcome the hypoxia-associated photodynamic resistance.

Therapeutic efficacy of HSA-MnO_2-Ce6 NPs in orthotopic bladder cancer model

Mice with orthotopic bladder cancer were divided into seven groups: PBS, HSA-MnO_2 NPs, HSA-MnO_2 NPs with laser irradiation, HSA-Ce6 NPs, HSA-MnO_2-Ce6 NPs, HSA-Ce6 NPs with laser

irradiation, and HSA-MnO_2-Ce6 NPs with laser irradiation. Tumor volumes of each group were ~120-130 mm^3 before treatments (Figure 7a). All groups showed an obvious solid lesion in the bladder before treatment as compared with normal bladders (Figure 7c). Bladders were irradiated by 660 nm laser for 15 min (200 mW/cm^2) after 24 h injection of the NPs (or PBS). The photodynamic effect of HSA-MnO_2-Ce6 NPs for bladder cancer was detected on day 3 by CEUS. Before treatment, bladder cancer presented as a low heterogeneous echo mass on ultrasonography, and CEUS showed a significant enhancement in the bladder cancer area (Figure 7b). After therapy, bladder cancer presented as a much lower echo mass on ultrasonography, with no obvious enhancement in bladder cancer area on day 3 because the tumor vessels and tissues were completely damaged by the enhanced PDT.

The therapeutic efficacy of HSA-MnO_2-Ce6 NPs-enhanced PDT was further evaluated by monitoring tumor size and weight. On day 12, the bladder cancer of mice treated with HSA-MnO_2-Ce6 NPs plus laser irradiation was significantly inhibited ($p=0.02$) (Figure 7a). This demonstrated the remarkably improved therapeutic efficacy as compared to other groups, including treatment with HSA-Ce6 NPs plus laser irradiation without the assistance of MnO_2 to reduce tumor hypoxia. As shown in Figure S7, the bladder weight of mice without the photodynamic effect (PBS, HSA-MnO_2 NPs, HSA-MnO_2 NPs with laser irradiation, HSA-Ce6 NPs, and HSA-MnO_2-Ce6 NPs) was significantly greater than those with the photodynamic effect (HSA-Ce6 and HSA-MnO_2-Ce6 NPs both with laser irradiation) because the photodynamic effect significantly decreased tumor volume. However, the bladder weight did not differ between HSA-Ce6 NPs and HSA-MnO_2-Ce6 NPs laser irradiation groups, probably due to incomplete absorption of damaged necrotic tumor tissue on the bladder on day 12.

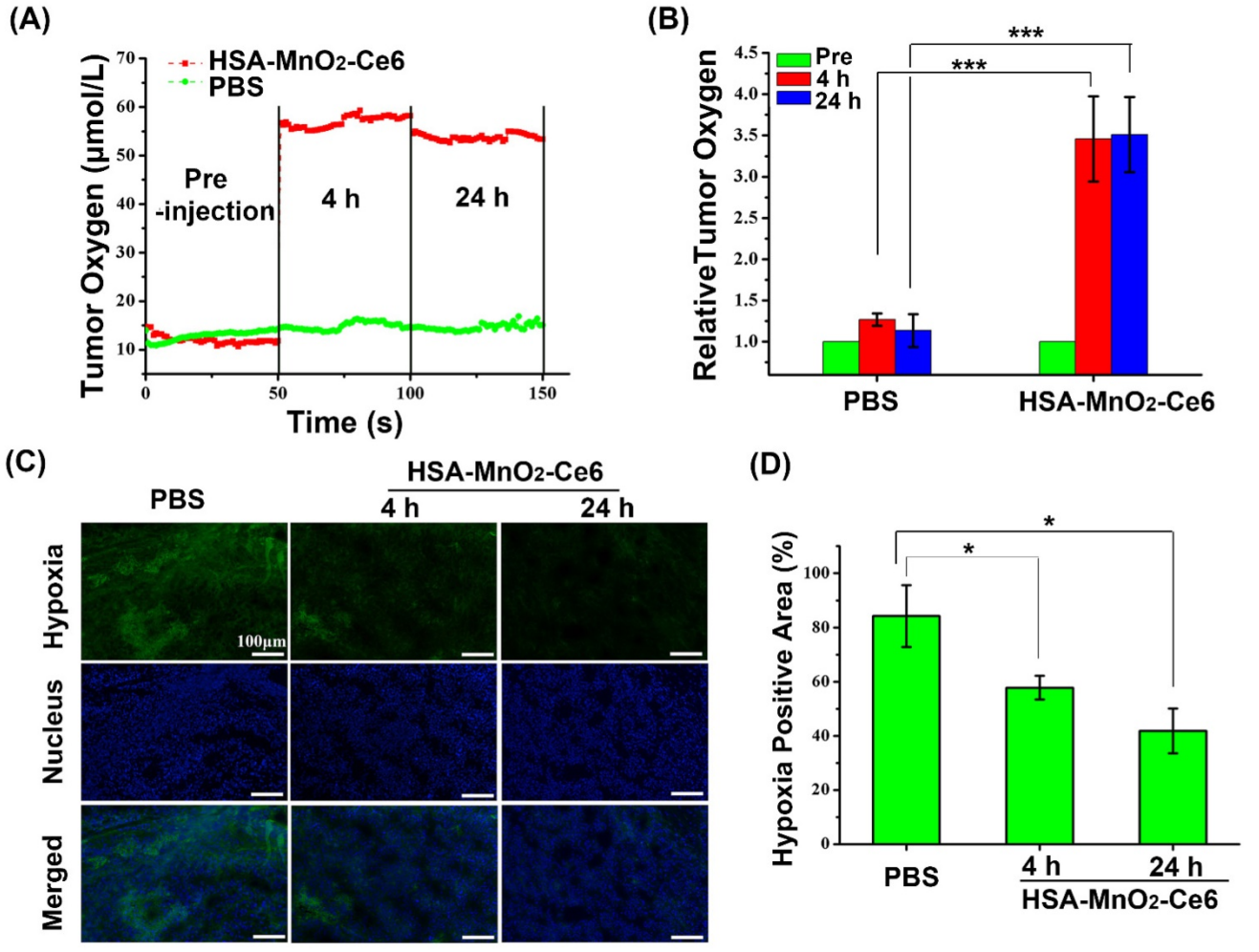

Figure 6. (a) O_2 concentration in tumor before and after intravenous injection of HSA-MnO_2-Ce6 NPs or PBS. (b) Tumor O_2 levels before and after treatment (***$p < 0.001$). (c) Representative immunofluorescence images of tumor slices after hypoxia staining. Cell nucleus and hypoxic areas were stained with DAPI (blue) and anti-pimonidazole antibody (green). (d) Relative tumor hypoxia-positive areas before and after treatment for 4 h and 24 h, determined from immunofluorescence images in (c) (*$p < 0.05$). Error bars indicate standard deviations of three independent measurements.

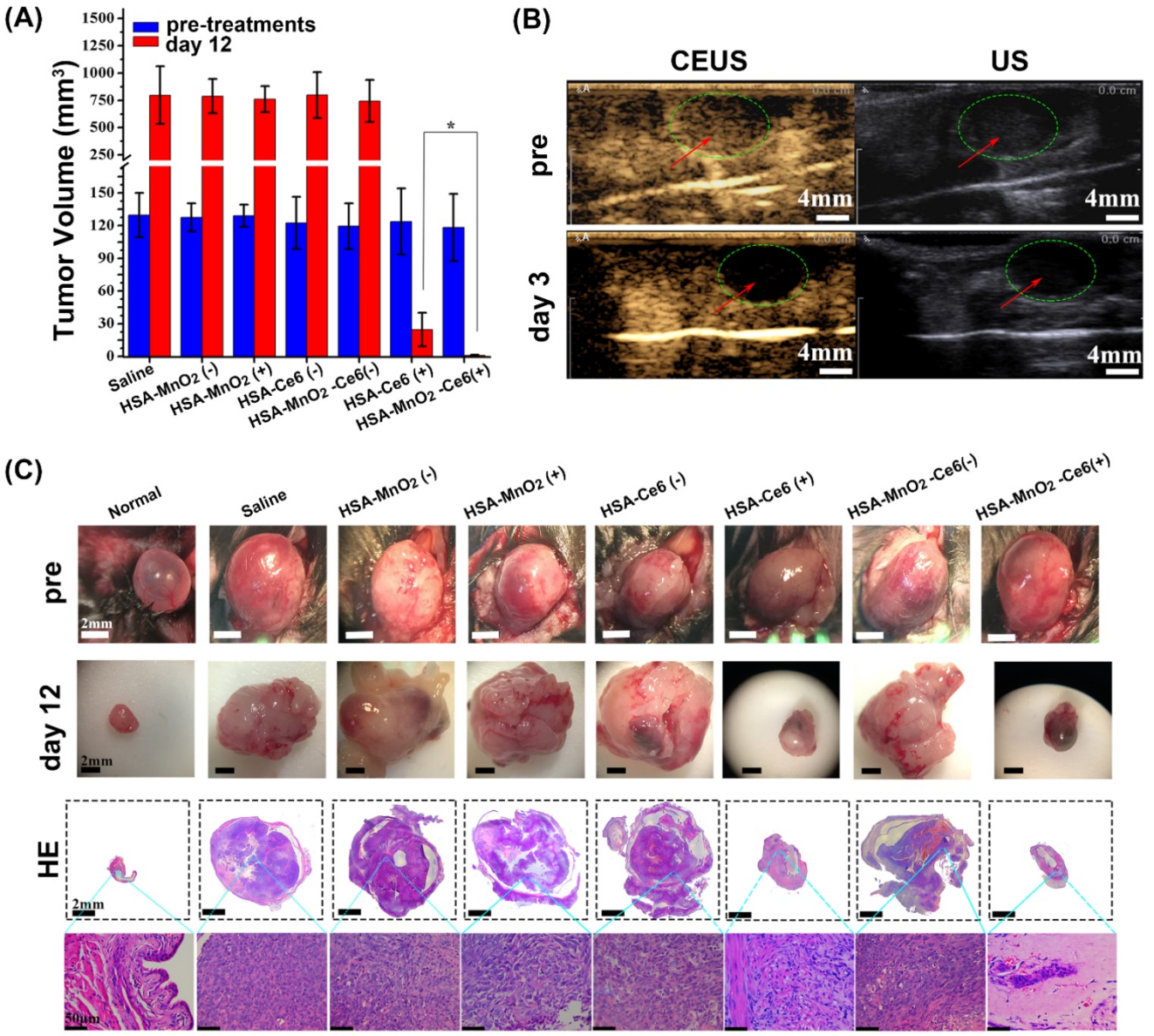

Figure 7. (a) Tumor volume before treatment and 12 days after treatment (bladders were exposed to 660 nm laser for 15 min (200 mW/cm^2)), (*$p<0.05$). (b) Photodynamic effect of HSA-MnO_2-Ce6 NPs on bladder cancer was detected pre-treatment and on day 3 by CEUS and US. (c) Representative images of orthotopic bladder cancers before and after treatments and corresponding HE-stained bladder sections. Error bars indicate standard deviations of four independent measurements.

The high-quality bladder images and pathological HE bladder slices on day 12 after treatments are shown in Figure 7c. The bladder volumes from HSA-Ce6 and HSA-MnO_2-Ce6 NPs laser irradiation groups were much smaller than those of the other five groups. This finding was due to the enormous space occupied by bladder lesions of the other five groups. The corresponding HE sections showed much larger residual bladder cancer areas in the HSA-Ce6 laser irradiation group than the HSA-MnO_2-Ce6 NPs laser irradiation group. Moreover, bladders from the HSA-MnO_2-Ce6 NPs laser irradiation group were similar to normal bladders. In the PBS, HSA-MnO_2 NPs, HSA-MnO_2 NPs with laser irradiation, HSA-Ce6 NPs, and HSA-MnO_2-Ce6 NPs groups, bladders were full of large lesions that invaded into all layers of the bladder wall and even grew outside of the bladder. Detailed bladder images for comparison of the photodynamic effect between HSA-Ce6 and HSA-MnO_2-Ce6 NPs are provided in Figure S8. The PDT treatment with HSA-MnO_2-Ce6 NPs conferred an obvious brown necrotic tissue in the residual bladder cancer area, but a solid residual tumor was observed with HSA-Ce6 NPs-based PDT treatment. Corresponding HE and TUNEL sections showed larger tumor necrosis area and more cell apoptosis with HSA-MnO_2-Ce6 NPs treatment, which suggested more complete tumor

damage with HSA-MnO_2-Ce6 NPs-enhanced photodynamic effect. In addition, the lifetime of mice was longer with HSA-MnO_2-Ce6 than HSA-Ce6 NPs treatment, both with laser irradiation (Figure 8). These results suggest that HSA-MnO_2-Ce6 NPs may be a powerful PDT agent, superior to HSA-Ce6 NPs, because HSA-MnO_2-Ce6 NPs significantly improved tumor hypoxia resulting from MnO_2-triggered H_2O_2 decomposition.

In vivo toxicity of HSA-MnO_2-Ce6 NPs

To evaluate the potential toxicity of HSA-MnO_2-Ce6 NPs treatment, the body weight loss of mice was used as an indicator for treatment-induced toxicity. The body weight of mice did not differ with various treatments (Figure 9a). To further assess the *in vivo* safety of HSA-MnO_2-Ce6 NPs, we analyzed blood samples and organs of healthy C57BL/6 mice injected with PBS or HSA-MnO_2-Ce6 NPs (5 mg/kg Ce6, 8.7 mg/kg MnO_2) on day 7 post-injection. Hepatic function was evaluated by ALT and AST levels and renal function by UREA and CREA levels. Levels of the four indicators did not differ between the two groups (Figure 9b). HE-stained sections of the five tissues (heart, liver, spleen, lung, and kidney) showed no apparent lesion (no necrosis, edema, inflammatory infiltration or hyperplasia) with PBS or the NPs injection (Figure 9c). These data suggested that PDT for orthotopic bladder cancer with HSA-MnO_2-Ce6 NPs treatment did not induce significant damage in major organs.

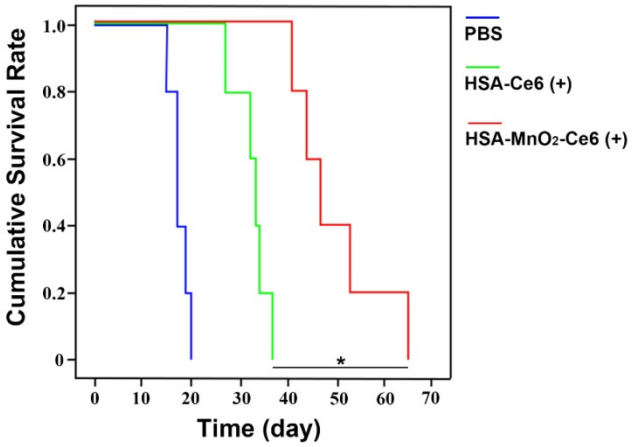

Figure 8. Cumulative survival rate of mice treated with PBS, HSA-Ce6 or HSA-MnO_2-Ce6 NPs under laser irradiation (*p<0.05). (n=5)

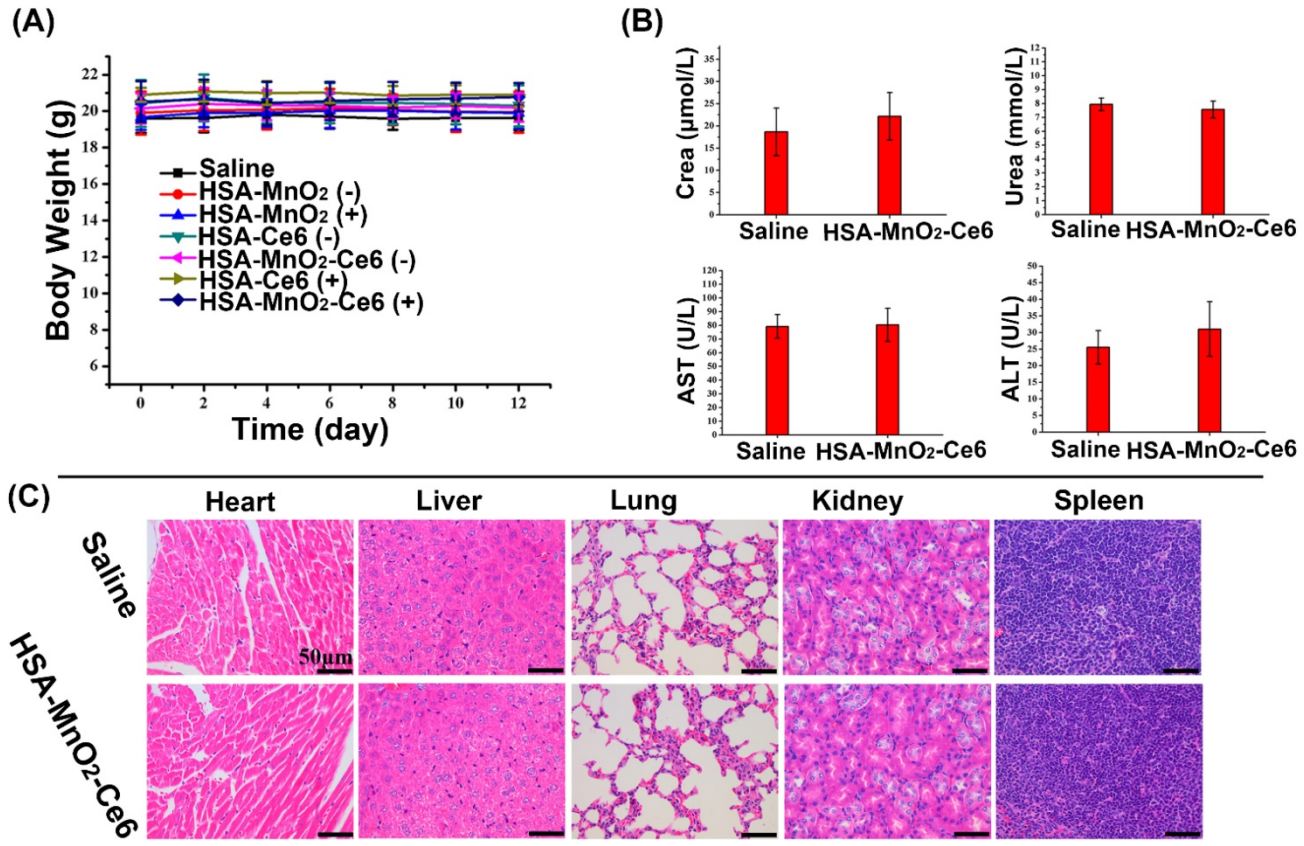

Figure 9. (a) Body weight of mice in different groups after treatments. (b) Hepatic function evaluated by ALT and AST levels and renal function by UREA and CREA levels. (c) HE staining of the five tissues (heart, liver, spleen, lung, and kidney). Error bars indicate standard deviations of four independent measurements.

Conclusions

In summary, we successfully fabricated O_2-generating HSA-MnO_2-Ce6 NPs for enhanced photodynamic effect to treat bladder cancer by overcoming hypoxia. HSA-MnO_2-Ce6 NPs have an excellent performance to generate O_2 in vitro upon reaction with H_2O_2 at endogenous levels. $^1O_2$ generation was two-fold higher with HSA-MnO_2-Ce6 NPs with the addition of H_2O_2 under 660-nm laser irradiation, which enhanced the PDT effect on bladder cancer cells. In vivo NIR and MR imaging suggested the excellent bladder tumor targeting property of HSA-MnO_2-Ce6 NPs. The tumor oxygen level increased ~3.5-fold after versus before injection of HSA-MnO_2-Ce6 NPs in orthotopic bladder cancer, which improved the tumor hypoxia condition in bladder cancer tissue significantly. Given the negligible toxicity of HSA-MnO_2-Ce6 NPs, they were further employed to treat orthotopic bladder cancer in mice combined with laser irradiation, showing remarkably improved therapeutic efficacy and significantly prolonged lifetime. The current study provides a promising strategy to design effective PDT agents for treating hypoxic bladder cancer. Moreover, in previous studies, subcutaneous tumor models were usually used. Here we used a more clinically relevant orthotopic bladder cancer model, which would have more clinical implications. Since hypoxia is a hallmark of most tumors, the currently developed method should be applicable to other tumors, which may help to address current clinical challenges.

Abbreviations

ALT: alanine aminotransferase; AST: aspartate aminotransferase; CCK-8: cell counting kit-8; CEUS: contrast enhanced ultrasound; Ce6: chlorin e6; CREA: creatinine; DAPI: 4',6-diamidino-2-phenylindole dihydrochloride; EDC: 1-ethyl-3-(3-dimethylamino-propyl) carbodiimide; H_2O_2: hydrogen peroxide; HSA: human serum albumin; $KMnO_4$: Potassium permanganate; MRI: magnetic resonance imaging; MnO_2: manganese dioxide; NHS: N-hydroxy-succinimide; NIR: near-infra-red; NPs: nanoparticles; O_2: oxygen; $^1O_2$: singlet oxygen; PBS: Phosphate buffer solution; PDT: Photodynamic therapy; RSI: relative signal intensity; SOSG: Singlet Oxygen Sensor Green; TEM: transmission electron microscopy; UREA: urea nitrogen; US: ultrasonography.

Supplementary Material

Figure S1-S11 and associated discussion, references.
http://www.thno.org/v08p0990s1.pdf

Acknowledgements

This work was supported by grants from the National Natural Science Foundation of China (nos. 81572519, 81502203, 81772710, 81602221, 21722503, and 21405081), the Social Development Project of Nanjing (201503014), the Natural Science Foundation of Jiangsu Province (BK20160117), the Jiangsu Province Medical Youth Talent (QNRC2016017) and the "Summit of the Six Top Talents" Program of Jiangsu Province (SWYY-084).

Competing Interests

The authors have declared that no competing interest exists.

References

1. Witjes JA, Comperat E, Cowan NC, et al. EAU Guidelines on Muscle-invasive and Metastatic Bladder Cancer: Summary of the 2013 Guidelines. *Eur Urol*. 2014;65(4):778-792.
2. Burger M, Catto JWF, Dalbagni G, et al. Epidemiology and Risk Factors of Urothelial Bladder Cancer. *Eur Urol*. 2013;63(2):234-241.
3. Witjes JA, Douglass J. The role of hexaminolevulinate fluorescence cystoscopy in bladder cancer. *Nat Clin Pract Urol*. 2007;4(10):542-549.
4. Antoni S, Ferlay J, Soerjomataram I, Znaor A, Jemal A, Bray F. Bladder Cancer Incidence and Mortality: A Global Overview and Recent Trends. *Eur Urol*. 2017;71(1):96-108.
5. Dolmans D, Fukumura D, Jain RK. Photodynamic therapy for cancer. *Nat Rev Cancer*. 2003;3(5):380-387.
6. Cheng L, Wang C, Feng LZ, Yang K, Liu Z. Functional Nanomaterials for Phototherapies of Cancer. *Chem Rev*. 2014;114(21):10869-10939.
7. Lucky SS, Soo KC, Zhang Y. Nanoparticles in Photodynamic Therapy. *Chem Rev*. 2015;115(4):1990-2042.
8. Zhang C, Zhao KL, Bu WB, et al. Marriage of Scintillator and Semiconductor for Synchronous Radiotherapy and Deep Photodynamic Therapy with Diminished Oxygen Dependence. *Angew Chem Int Ed*. 2015;54(6):1770-1774.
9. Lu KD, He CB, Lin WB. A Chlorin-Based Nanoscale Metal-Organic Framework for Photodynamic Therapy of Colon Cancers. *J Am Chem Soc*. 2015;137(24):7600-7603.
10. Ge JC, Lan MH, Zhou BJ, et al. A graphene quantum dot photodynamic therapy agent with high singlet oxygen generation. *Nat Commun*. 2014;5:4596.
11. Fan W, Huang P, Chen X. Overcoming the Achilles' heel of photodynamic therapy. *Chem Soc Rev*. 2016;45(23):6488-6519.
12. Punjabi A, Wu X, Tokatli-Apollon A, et al. Amplifying the Red-Emission of Upconverting Nanoparticles for Biocompatible Clinically Used Prodrug-Induced Photodynamic Therapy. *ACS Nano*. 2014;8(10):10621-10630.
13. Lu K, He C, Lin W. A Chlorin-Based Nanoscale Metal-Organic Framework for Photodynamic Therapy of Colon Cancers. *J Am Chem Soc*. 2015;137(24):7600-7603.
14. Li Y, Wen T, Zhao R, et al. Localized Electric Field of Plasmonic Nanoplatform Enhanced Photodynamic Tumor Therapy. *Acs Nano*. 2014;8(11):11529-11542.
15. Zhen ZP, Tang W, Chuang YJ, et al. Tumor Vasculature Targeted Photodynamic Therapy for Enhanced Delivery of Nanoparticles. *ACS Nano*. 2014;8(6):6004-6013.
16. Li W, Zheng C, Pan Z, et al. Smart hyaluronidase-actived theranostic micelles for dual-modal imaging guided photodynamic therapy. *Biomaterials*. 2016;101:10-19.
17. Celli JP, Spring BQ, Rizvi I, et al. Imaging and Photodynamic Therapy: Mechanisms, Monitoring, and Optimization. *Chem Rev*. 2010;110(5):2795-2838.
18. Nomoto T, Fukushima S, Kumagai M, et al. Calcium phosphate-based organic-inorganic hybrid nanocarriers with pH-responsive on/off switch for photodynamic therapy. *Biomater Sci*. 2016;4(5):826-838.
19. Wang GD, Nguyen HT, Chen HM, et al. X-Ray Induced Photodynamic Therapy: A Combination of Radiotherapy and Photodynamic Therapy. *Theranostics*. 2016;6(13):2295-2305.
20. Song XJ, Feng LZ, Liang C, Gao M, Song GS, Liu Z. Liposomes co-loaded with metformin and chlorin e6 modulate tumor hypoxia during enhanced photodynamic therapy. *Nano Res*. 2017;10(4):1200-1212.
21. Park Y, Kim HM, Kim JH, et al. Theranostic Probe Based on Lanthanide-Doped Nanoparticles for Simultaneous In Vivo Dual-Modal Imaging and Photodynamic Therapy. *Adv Mater*. 2012;24(42):5755-5761.
22. Cheng H, Zhu JY, Li SY, et al. An O_2 Self-Sufficient Biomimetic Nanoplatform for Highly Specific and Efficient Photodynamic Therapy. *Adv Funct Mater*. 2016;26(43):7847-7860.

23. Chen Q, Xu L, Liang C, Wang C, Peng R, Liu Z. Photothermal therapy with immune-adjuvant nanoparticles together with checkpoint blockade for effective cancer immunotherapy. *Nat Commun*. 2016;7:13193.
24. Lin TY, Li YP, Liu QQ, et al. Novel theranostic nanoporphyrins for photodynamic diagnosis and trimodal therapy for bladder cancer. *Biomaterials*. 2016;104:339-351.
25. Inoue K. 5-Aminolevulinic acid-mediated photodynamic therapy for bladder cancer. *Int J Urol*. 2017;24(2):97-101.
26. Lee JY, Diaz RR, Cho KS, et al. Efficacy and Safety of Photodynamic Therapy for Recurrent, High Grade Nonmuscle Invasive Bladder Cancer Refractory or Intolerant to Bacille Calmette-Guerin Immunotherapy. *J Urol*. 2013;190(4):1192-1199.
27. Bader MJ, Stepp H, Beyer W, et al. Photodynamic Therapy of Bladder Cancer - A Phase I Study Using Hexaminolevulinate (HAL). *Urol Oncol-Semin Orig Investig*. 2013;31(7):1178-1183.
28. Black PC, Shetty A, Brown GA, et al. Validating bladder cancer xenograft bioluminescence with magnetic resonance imaging: the significance of hypoxia and necrosis. *BJU International*. 2010;106(11):1799-1804.
29. Blick C, Ramachandran A, Wigfield S, et al. Hypoxia regulates FGFR3 expression via HIF-1 alpha and miR-100 and contributes to cell survival in non-muscle invasive bladder cancer. *Br J Cancer*. 2013;109(1):50-59.
30. Hunter BA, Eustace A, Irlam JJ, et al. Expression of hypoxia-inducible factor-1 alpha predicts benefit from hypoxia modification in invasive bladder cancer. *Br J Cancer*. 2014;111(3):437-443.
31. Maier A, Anegg U, Tomaselli F, et al. Does hyperbaric oxygen enhance the effect of photodynamic therapy in patients with advanced esophageal carcinoma? A clinical pilot study. *Endoscopy*. 2000;32(1):42-48.
32. Cheng YH, Cheng H, Jiang CX, et al. Perfluorocarbon nanoparticles enhance reactive oxygen levels and tumour growth inhibition in photodynamic therapy. *Nat Commun*. 2015;6:8785.
33. Chen HC, Tian JW, He WJ, Guo ZJ. H_2O_2-Activatable and O_2-Evolving Nanoparticles for Highly Efficient and Selective Photodynamic Therapy against Hypoxic Tumor Cells. *J Am Chem Soc*. 2015;137(4):1539-1547.
34. Liu CP, Wu TH, Liu CY, et al. Self-Supplying O_2 through the Catalase-Like Activity of Gold Nanoclusters for Photodynamic Therapy against Hypoxic Cancer Cells. *Small*. 2017;13(26): 1700278.
35. Gao S, Wang G, Qin Z, et al. Oxygen-generating hybrid nanoparticles to enhance fluorescent/photoacoustic/ultrasound imaging guided tumor photodynamic therapy. *Biomaterials*. 2017;112:324-335.
36. Zhu W, Dong Z, Fu T, et al. Modulation of hypoxia in solid tumor microenvironment with MnO_2 nanoparticles to enhance photodynamic therapy. *Adv Funct Mater*. 2016;26(30):5490-5498.
37. Fan H, Yan G, Zhao Z, et al. A smart photosensitizer–manganese dioxide nanosystem for enhanced photodynamic therapy by reducing glutathione levels in cancer cells. *Angew Chem*. 2016;128(18):5567-5572.
38. Shimada K, Nakamura M, Anai S, et al. A Novel Human AlkB Homologue, ALKBH8, Contributes to Human Bladder Cancer Progression. *Cancer Res*. 2009;69(7):3157-3164.
39. Lopez-Lazaro M. Dual role of hydrogen peroxide in cancer: Possible relevance to cancer chemoprevention and therapy. *Cancer Lett*. 2007;252(1):1-8.
40. Chiche J, Brahimi-Horn MC, Pouyssegur J. Tumour hypoxia induces a metabolic shift causing acidosis: a common feature in cancer. *J Cell Mol Med*. 2010;14(4):771-794.
41. Martinez-Outschoorn UE, Lin Z, Trimmer C, et al. Cancer cells metabolically "fertilize" the tumor microenvironment with hydrogen peroxide, driving the Warburg effect Implications for PET imaging of human tumors. *Cell Cycle*. 2011;10(15):2504-2520.
42. Ma ZF, Jia XD, Bai J, et al. MnO_2 Gatekeeper: An Intelligent and O_2-Evolving Shell for Preventing Premature Release of High Cargo Payload Core, Overcoming Tumor Hypoxia, and Acidic H_2O_2-Sensitive MRI. *Adv Funct Mater*. 2017;27(4):1604258.
43. Tian LL, Chen Q, Yi X, et al. Albumin-Templated Manganese Dioxide Nanoparticles for Enhanced Radioisotope Therapy. *Small*. 2017;13(25):1700640.
44. Chen Q, Feng LZ, Liu JJ, et al. Intelligent Albumin-MnO_2 Nanoparticles as pH-/H_2O_2-Responsive Dissociable Nanocarriers to Modulate Tumor Hypoxia for Effective Combination Therapy. *Adv Mater*. 2016;28(33):7129-7136.
45. Gordijo CR, Abbasi AZ, Amini MA, et al. Design of Hybrid MnO_2-Polymer-Lipid Nanoparticles with Tunable Oxygen Generation Rates and Tumor Accumulation for Cancer Treatment. *Adv Funct Mater*. 2015;25(12):1858-1872.
46. Ho CJH, Balasundaram G, Driessen W, et al. Multifunctional Photosensitizer-Based Contrast Agents for Photoacoustic Imaging. *Sci Rep*. 2014;4:5342.
47. Kamkaew A, Lim SH, Lee HB, Kiew LV, Chung LY, Burgess K. BODIPY dyes in photodynamic therapy. *Chem Soc Rev*. 2013;42(1):77-88.
48. Chen Q, Liu Z. Albumin Carriers for Cancer Theranostics: A Conventional Platform with New Promise. *Adv Mater*. 2016;28(47):10557-10566.
49. Kratz F. A clinical update of using albumin as a drug vehicle - A commentary. *J Control Release*. 2014;190:331-336.
50. Pan JB, Wang YQ, Pan HY, et al. Mimicking Drug-Substrate Interaction: A Smart Bioinspired Technology for the Fabrication of Theranostic Nanoprobes. *Adv Funct Mater*. Jan 2017;27(3):1603440.
51. Lin TS, Yuan A, Zhao XZ, et al. Self-assembled tumor-targeting hyaluronic acid nanoparticles for photothermal ablation in orthotopic bladder cancer. *Acta Biomater*. 2017;53:427-438.
52. Otto GP, Rathkolb B, Oestereicher MA, et al. Clinical Chemistry Reference Intervals for C57BL/6J, C57BL/6N, and C3HeB/FeJ Mice (Mus musculus). *J Am Assoc Lab Anim Sci*. 2016;55(4):375-386.
53. Jeong H, Huh M, Lee SJ, et al. Photosensitizer-Conjugated Human Serum Albumin Nanoparticles for Effective Photodynamic Therapy. *Theranostics*. 2011;1:230-239.
54. Luo YL. Preparation of MnO_2 nanoparticles by directly mixing potassium permanganate and polyelectrolyte aqueous solutions. *Mater Lett*. 2007;61(8-9):1893-1895.
55. Ghosh D, Lee Y, Thomas S, et al. M13-templated magnetic nanoparticles for targeted in vivo imaging of prostate cancer. *Nat Nanotechnol*. 2012;7(10):677-682.
56. Chen Y, Ye DL, Wu MY, et al. Break-up of Two-Dimensional MnO_2 Nanosheets Promotes Ultrasensitive pH-Triggered Theranostics of Cancer. *Adv Mater*. 2014;26(41):7019-7026.